Computational Materials Science 138 (2017) 183–191

Contents lists available at ScienceDirect

Computational Materials Science

journal homepage: www.elsevier.com/locate/commatsci

Linear-parabolic transition in reactive diffusion – A concept of kinetic modelling

J.J. Tomán [a,*], G. Schmitz [b], Z. Erdélyi [a]

[a] Department of Solid State Physics, University of Debrecen, P.O. Box 400, H-4002 Debrecen, Hungary
[b] Institute of Materials Science, University of Stuttgart, Heisenbergstr. 3, 70569 Stuttgart, Germany

ARTICLE INFO

Article history:
Received 6 October 2016
Received in revised form 31 March 2017
Accepted 8 June 2017

Keywords:
Reactive diffusion
Solid state reaction
Linear-parabolic kinetics
Continuum model

ABSTRACT

In Erdélyi and Schmitz (2012) a flexible concept for the computational description of the phase formation and growth in solid state reactions was described. Unlike in other established approaches, it is not required to predefine and trace phase boundaries by dividing surfaces or similar concepts. We show how to extend the concept to the transition between linear to parabolic growth kinetics. Although no interphase boundaries are predefined, it is nevertheless possible to correctly describe the impact of interfacial transport barriers. This allows a transparent modelling of the linear-parabolic transitions in reactive diffusion.

1. Introduction

In established computational approaches to the diffusional processes of phase separation or interreaction, it is common practice to describe the appearing phase boundaries by some kind of dividing interfaces. The fluxes to both sides of the interface are evaluated in a dedicated manner to predict the migration of the boundary and so to allow the book-keeping of its momentary position, see e.g. [1] or [2]. In a recent work [3], we used an alternative concept of simulating reactive diffusion that avoided the mentioned book-keeping of the interfaces. Based on the appropriate thermodynamic driving forces, expressed by correct thermodynamic factors of chemical potentials, the algorithm predicts the phase transformations automatically, a concept that has been already discussed earlier [4]. But in contrast to this earlier report, now phase boundaries are not assigned to dividing interfaces anymore, but are simply related to volume slabs revealing a composition inside the forbidden concentration range of the two-phase regions. At first sight, this concept appears to be just a formal computational trick. However, focusing on nanodevices, it may even become the more realistic picture. A phase boundary cannot be infinitely sharp but may have a thickness of about a nanometer at least. So, the interface-related volume becomes significant in comparison to the total volume of a nanodevice.

In this article we develop and demonstrate how to describe the transition from linear to parabolic kinetics within the proposed computational concept. In phenomenological understanding of phase growth by solid state reaction, it is usually supposed that transfer of atoms through phase boundaries is hindered by different reasons. Whatever the reason is, extra potential barriers are supposed to be present at the phase boundaries which slow down the atomic transport [5,6]. Introduced as a concept of describing the kinetics of gas reactions, such as oxidation [7], the concept of linear growth was transferred to solid state reactions whenever a kinetic control by the interfaces had to be presumed [8,9]. While to the best of our knowledge no clear and undisputed case of linear interdiffusion kinetics has been reported for the reaction of pure metals (perhaps [10]), apparently clear experimental confirmations do exist for silicide reactions, e.g. [11–14]. A. Gusak [15] has presented arguments that a linear kinetic regime can hardly be observed in metallic thin films, provided sufficiently efficient vacancy sinks and sources. However, he also showed that non-equilibrium vacancies, eventually also other point defects, could force a significant linear regime at the transition between the early slow *Nernst – Planck* interdiffusion stage and the later fast *Darken* interdiffusion. So, the concept of linear growth seems to be relevant, even more so as it finds renewed interest in recent work on reactive diffusion in nanowires [16].

Our article is structured as follows. First, the basic concept of the suggested transport simulation is summarized. Then, in order to check its quantitative correctness, we derive an independent analytical solution of the reactive diffusion problem that can be

* Corresponding author.
E-mail address: janos.toman@science.unideb.hu (J.J. Tomán).
URL: http://ssphys.science.unideb.hu (J.J. Tomán).

http://dx.doi.org/10.1016/j.commatsci.2017.06.009
0927-0256/

applied to any arbitrary binary phase diagrams. A comparison with this innovative analytical solution confirms the validity of the kinetic simulation. But it also demonstrates deviations in early stages which gives rise to the main aim of this article, the modification of the kinetic concept to even simulate the effect of barriers at interfaces. Quantitative accuracy of this modification is demonstrated by comparison with the approximate description by Deal and Grove [7]. Finally, we demonstrate the flexible use of the simulation in describing complex cases comprising different relevant interfaces.

2. Basic equations of the kinetic simulation model

The following basic equations for numerical simulation were derived in Ref. [3] in the context of studying elastic stress and plastic relaxation in core shell nanostructures. For clarity, we repeat them here in a reduced form that is sufficient to describe the atomic transport by a vacancy mechanism, but disregarding the influence of mechanical forces.

2.1. Continuum equations of atomic transport

In order to calculate the change of composition in time and space by vacancy mediated diffusion, the equation

$$\frac{\mathrm{D}c_i}{\mathrm{D}t} = -\frac{1}{\rho}\nabla' \vec{j}_i - c_i s_v \quad \text{for } i = 1,\ldots,n, \tag{1}$$

is used for all n atomic components. The differential $\mathrm{D}/\mathrm{D}t$ is known as the *substantial (or material) derivative*. It gives the rate of change of any scalar quantity seen at a point which follows the motion of the material coordinate system. Moreover $\vec{j}_i$ is the flux of component i, ρ is the total material density (number of lattice sites per volume), c_i is the atomic fraction of component i, ∇' indicates the *divergent* calculated in the material coordinate system (see e.g. [3]), and s_v gives the rate of change of the atomic fraction of vacancies due to creation/annihilation.

The total material density can be calculated from the partial material densities of the components i (ρ_i) and that of the vacancies (ρ_v): $\rho = \sum_{i=1}^{n}\rho_i + \rho_v$. Consequently, atomic fractions are related to the material densities by

$$c_i = \frac{\rho_i}{\rho} \quad \text{for } i = 1,\ldots,n \text{ and } i = v. \tag{2}$$

In turn, the total density ρ can also be expressed in terms of partial atomic volumes

$$\rho = \frac{1}{\sum_{i=1}^{n} c_i\Omega_i + c_v\Omega_v}. \tag{3}$$

The rate of vacancy creation/annihilation at a source/sink is considered to be proportional to the deviation of the current fraction of vacancies from the equilibrium one

$$s_v = K_{rate}\left(c_v^0 - c_v\right), \tag{4}$$

where the rate coefficient K_{rate} determines the effectiveness of sinks and sources. We emphasise that K_{rate} is not necessarily a constant but may vary, for instance, with spatial coordinates depending on the spatial distribution of the sinks and sources [17]. Note that other expression for s_v can be also used. See for instance in [18,19]. However, the present work is not intended to investigate the role of the different expressions for s_v.

In the case of a vacancy diffusion mechanism, the flux of component i can be written as [3,20]

$$\vec{j}_i = -\rho\frac{\mathscr{D}_i}{\mathrm{k}T}c_v c_i\left(\nabla'\mu_i - \nabla'\mu_v\right) \quad \text{for } i = 1,\ldots,n, \tag{5}$$

in which we have conveniently defined $\mathscr{D}_i = D_i^*/c_v^0$, with D_i^* being the tracer diffusion coefficient of the chemical component i [3,21]; k and T are Botzmann's constant and the absolute temperature. Furthermore, μ_i and μ_v are chemical potentials of component i and of the vacancy.

For the remaining of this article, we restrict to binary A-B alloys. If local equilibrium is fulfilled, the chemical potentials behave continuous. In this case Eq. (5) may also be expressed as

$$\vec{j}_i = -\rho\mathscr{D}_i\left(\Theta_i c_v\nabla' c_i - \Theta_v c_i\nabla' c_v\right) \quad \text{for } i = A,B \tag{6}$$

with the usual thermodynamic factors $\Theta_A = (\partial\mu_A/\partial\ln c_A)/\mathrm{k}T = \Theta_B$. It should be emphasized that Eqs. (5) and (6) are mathematically equivalent for a binary system. Therefore, in contrast to a recent critizism [22,23], it is always possible to derive suitable discretisation schemes for both variants so that identical results are achieved in numerical calculation.

If vacancy sinks and sources are so efficient that vacancy equilibrium holds (usually assumed for macroscopic systems), both variants of the transport equation may be further simplified:

$$\vec{j}_i = -\rho\frac{D_i^*}{\mathrm{k}T}c_i\nabla'\mu_i = -\rho D_i^*\Theta_i\nabla' c_i; \text{ for } i = A,B \tag{7}$$

and the sink term in Eq. (1) is neglected. Furthermore, mixing of the two components in the laboratory reference frame can then be described by a single exchange flux $\tilde{j} := j_A - c(j_A + j_B)$ Here and in the following c shall denote the atomic fraction of component A. The relevant driving force becomes the exchange potential $\tilde{\mu} := \mu_A - \mu_B$ so that the appropriate transport equation reads

$$\tilde{j} = \rho\frac{\widetilde{D}}{\mathrm{k}T}c(1-c)\nabla\tilde{\mu}, \tag{8}$$

with the interdiffusion coefficient

$$\widetilde{D}(c) = D_A^*(1-c) + D_B^* c. \tag{9}$$

2.2. Chemical driving forces

As a demonstration example, we consider a binary A-B systems that forms a single intermetallic phase, which stands in equilibrium to ideal solid solutions at both terminating sides of the phase diagram.

The Gibbs energy of mixing of an ideal binary solid solution (SS) is natural, while the Gibbs energy of the intermetallic phase (IM) shall be approximated by a second order polynomial, so

$$\begin{aligned} g^{SS} &= \mathrm{k}T[c\ln c + (1-c)\ln(1-c)], \\ g^{IM} &= -g_0 + V(c-c_m)^2. \end{aligned} \tag{10}$$

Here c_m denotes the stoichiometric concentration of component A in the intermetallic phase, and g_0 and V are parameters by which the existence range of the intermetallic phase can be adjusted.

With this, the chemical potentials of component A for the solid solution and the intermetallic phases are

$$\begin{aligned} \mu_A^{SS} &= \mathrm{k}T\ln c, \\ \mu_A^{IM} &= -g_0 + V\left(-c^2 + c_m^2 + 2c - 2c_m\right). \end{aligned} \tag{11}$$

As in the composition range $0\ldots c_1$ the solid solution is stable, the chemical potential is calculated from μ_A^{SS}; in the range $c_2\ldots c_3$, the intermetallic compound is the stable phase, so μ is calculated from μ_A^{IM}; and in the range $c_4\ldots 1$, it is calculated again from μ_A^{SS}. In the two-phase ranges $c_1\ldots c_2$ and $c_3\ldots c_4$, the chemical potential remains constant and equals to $\mu_A(c_1)$ and $\mu_A(c_3)$ calculated form either μ_A^{SS} or μ_A^{IM} (for the definition of the boundary con-

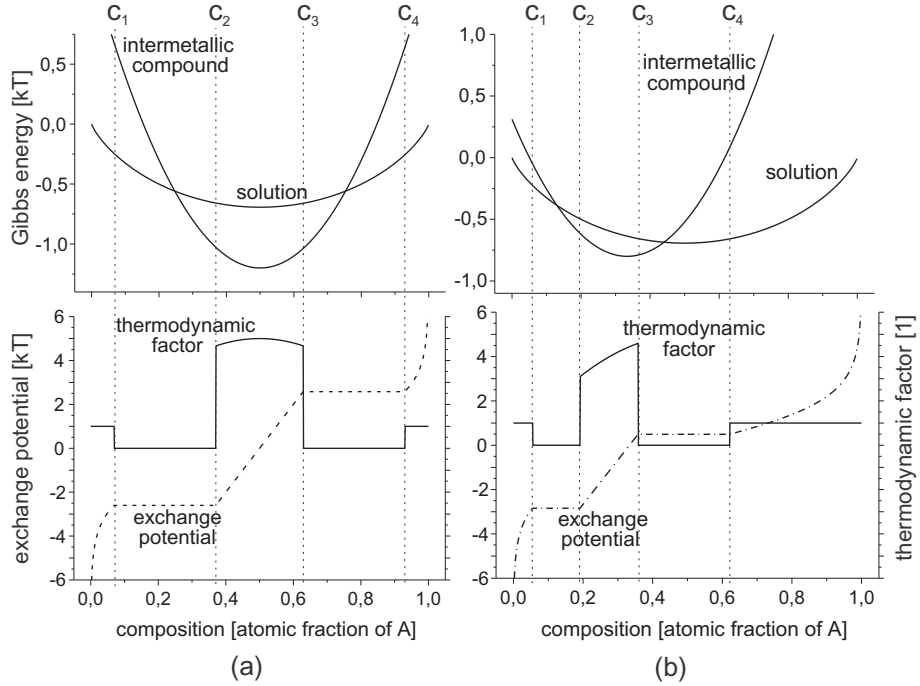

Fig. 1. Thermodynamic driving forces of assumed symmetric phase diagram comprising an AB compound (a) and of an asymmetric phase diagram with an A_2B compound (b). Upper panels show the Gibbs potentials of the phases, lower panels the respective exchange (interdiffusion) potential and the thermodynamic factor. c_1 to c_4 denote equilibrium compositions of the phase boundaries. (Parameters for the AB compound: $c_m = 0.500$, $g_0/\mathrm{kT} = 1.2$ and $V/\mathrm{kT} = 10$, for the A_2B compound: $c_m = 0.333$, $g_0/\mathrm{kT} = 0.8$ and $V/\mathrm{kT} = 10$).

centrations c_1 to c_4 see Fig. 1. Equivalently, we may set in the two-phase ranges the thermodynamic factor $\Theta_A = 0$. The analogous considerations hold for component B.

We will perform calculations for two cases, a symmetric and an asymmetric phase diagram as shown in Fig. 1(a,b). For both the Gibbs potentials, the exchange potential, and the thermodynamic factor are presented. Respective parameters used in Eq. (10) are stated in the figure caption.

The equations given in Sections 2.1 and 2.2 fully describe the kinetic model used for simulation. (Further technical information on the numerical implementation is summarized in Appendix A.) It must be pointed out that the modelling avoids any predefined interfaces of which the positions have to be tracked and at which the equilibrium conditions are maintained by a particular treatment. All required physical information is contained in the composition dependence of the chemical potentials or thermodynamic factors together with the composition dependence of the intrinsic diffusion coefficients. Interfaces are simply identified by a local composition falling into the two-phase regions, and are consequently marked by constant chemical potentials respectively a vanishing thermodynamic factor.

3. Analytical solution of the reactive diffusion problem

Since the simulation algorithm outlined in Section 2 was recently criticised for failing even in prediction of simple parabolic growth [22,23], a demonstration of its accuracy is required. To this aim, we need an alternative analytical solution of the binary reactive diffusion problem, to which we could compare the results of the kinetic simulation. Often, the rate of compound growth in reactive diffusion is estimated on the assumption of a linear concentration profile and a constant flux across the forming intermetallic layer (see e.g. [24,15]). With this, the temporal evolution of the compound layer width w is predicted as

$$w\frac{dw}{dt} = \widetilde{D}\left(\frac{c_3 - c_2}{c_4 - c_3} + \frac{c_3 - c_2}{c_2 - c_1}\right). \tag{12}$$

(The boundary compositions c_i are assigned as in Fig. 1 and $\widetilde{D}$ represents an average interdiffusion coefficient of the intermetallic phase.)

In steady state of transport however, not both current and gradient of concentration can be constant. Therefore, Eq. (12) only represents a rough estimate. In the following, we derive therefore an exact analytical solution to predict the composition profile for any arbitrary binary phase diagram and concentration dependence of the chemical interdiffusion coefficient.

We start from the known fact of general parabolic growth in the diffusion zone. Therefore, conservation of matter requires

$$\frac{\partial c}{\partial t} = -\frac{x}{2t}\cdot\frac{\partial c}{\partial x} = -\frac{1}{\rho}\frac{\partial \tilde{j}}{\partial x}, \tag{13}$$

if the origin of the space coordinate x is located at the Matano plane. Multiplying by $\widetilde{D}(c)$ and obeying Fick's first law ($\tilde{j} = -\rho\widetilde{D}(\partial c/\partial x)$), we find from Eq. (13)

$$\widetilde{D}(c)\frac{\partial \tilde{j}}{\partial x} = -\frac{x}{2t}\tilde{j}. \tag{14}$$

If here $\widetilde{D}$ were constant, a simple Gaussian solved Eq. (14):

$$\tilde{j}(x) = j_M \exp\left[-\frac{x^2}{4\widetilde{D}t}\right], \tag{15}$$

which represents nothing else than the well-known error-function-shaped diffusion profile. Guided by this observation, we define for the case of a composition dependent $\widetilde{D}(c)$ a new depth coordinate u by

$$u\mathrm{d}u := \frac{x}{\widetilde{D}(c)}\mathrm{d}x \tag{16}$$

while keeping the origin at the Matano plane $u(x=0)=0$. The advantage of this new coordinate becomes obvious in noting by combination of Eqs. (13) and (16), and Fick's first law

$$\frac{\partial \tilde{j}}{\partial u} = \frac{u}{x}\tilde{D}\frac{\partial \tilde{j}}{\partial x} = \frac{u}{x}\tilde{D}\frac{x}{2t}\frac{\partial c}{\partial x} = -\frac{u}{2t}\tilde{j}. \tag{17}$$

Obviously, as a function of the new coordinate u, the flux becomes Gaussian-shaped again

$$\tilde{j}(u) = j_M \cdot \exp\left(-\frac{u^2}{4t}\right). \tag{18}$$

So, beginning from the Matano plane ($x=u=0;\ c=c_M;\ \tilde{j}=j_M$), we may calculate the concentration profile at given time by simultaneous integration of

$$du = \frac{x}{u}\frac{dx}{\tilde{D}} = \frac{x}{u}\frac{dx}{dc}\frac{dc}{\tilde{D}} = \frac{x}{u\tilde{j}(u)}\,dc \tag{19}$$

$$dx = \frac{\partial x}{\partial c}dc = \frac{\tilde{D}(c)}{\tilde{j}(u)}\,dc \tag{20}$$

with regard to Eq. (18). (Details on the implementation by the "shooting" method to solve a boundary value problem are detailed in Appendix B.)

4. Check of the quantitative accuracy of the kinetic simulation

To demonstrate the quantitative correctness of the simulation concept, we consider interdiffusion in binary systems based on the Gibbs potentials shown in Fig. 1. Partial diffusion coefficients and atomic volumes are assumed being equal for both components. Thus, the vacancy density is in equilibrium and the calculation can be handled on a fixed periodic discretisation grid of spacing a_0. We emphasise, these assumptions are not required for the concept to work. The use of composition dependent partial diffusion coefficients and non-uniform distribution of vacancy sinks and sources were already demonstrated in this model [17,25]. The simpler assumptions here, though, make the quantitative evaluation possible throughout this work. We simulate the evolution of 1D diffusion profiles by the kinetic equations presented in Section 2 (Eq. (7)) and determine the width of the intermetallic product as a function of time. Then, we compare with the exact analytic solution according to Section 3.

Exemplary results of such comparison are presented in Fig. 2, data points stem from the kinetic simulation, lines from the analytical calculation. Obviously, the concentration profiles match perfectly, only with exception of the grid points directly at the phase boundaries.

A detailed quantitative evaluation is presented in Fig. 3. Partial figure (a) shows the width of the intermetallic compound as a function of time, data points stem from the kinetic simulation, dashed lines from the analytical solution. Both are in perfect agreement, if the width of the intermetallic compound exceeds about 20 units of the simulation grid (a_0). Note, there is no free fitting parameter to match both models. The kinetic simulation concept reproduces the expected parabolic growth with correct absolute growth rate for the symmetric AB and the asymmetric A_2B compound as well and so is well confirmed.

On the other hand, Fig. 3(a) makes it obvious that the growth rate predicted by the kinetic simulation falls short of the expected parabolic one, if the compound layers are very thin. Similarly the equilibrium boundary concentrations are not established for rather thin layers as demonstrated in Fig. 3(b). Since this behaviour resembles to the physical feature of a transport barrier at the interfaces, we investigate in the following, whether we can turn this apparent shortcoming of the kinetic model even into an advantage.

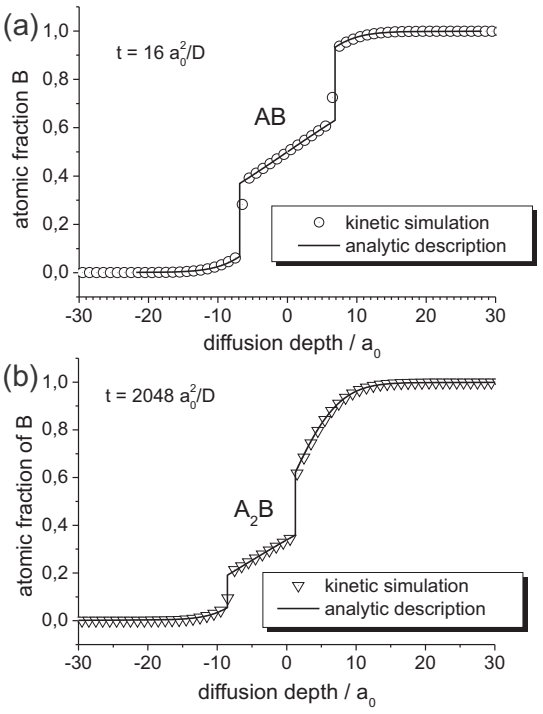

Fig. 2. Comparison of concentration profiles across the diffusion zone as determined by kinetic simulation (data points) and analytic calculation (solid lines) for the symmetric (a) and the asymmetric phase diagram (b). (The Matano plane is located at zero depth.)

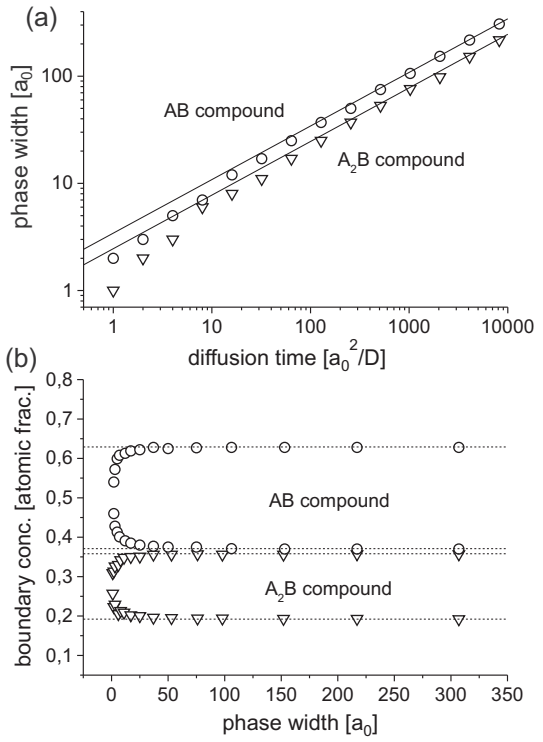

Fig. 3. Comparison of kinetic simulation (data points) and analytic description (lines) of intermetallic phase growth. (a) Width of the AB (circles) and A_2B (triangles) intermetallic layer versus diffusion time; (b) boundary concentrations of the intermetallic compounds in comparison to phase boundaries of the underlying phase diagrams (dashed).

To this aim, we first remind to the concept of interfacial transport barriers and the linear–to–parabolic transition in layer growth. Afterwards we generalize the simulation tool accordingly.

5. Linear-parabolic transition in kinetics of layer growth

5.1. Phenomenological approach

One of the earliest and most accepted descriptions of the growth of a reaction product was early proposed by Deal and Grove for the case of the oxidation of Si [7]. They supposed that the flux across a phase boundary is proportional to the difference between the actual and equilibrium concentrations at the phase boundaries. Moreover, they assumed the flux being constant inside the growing phase. Following the arguing in Section 3, the latter can be valid only for a strict line compound.

We consider a growing compound layer embedded between two terminating solutions of the respective equilibrium compositions (c_1, c_4). The relevant driving forces are illustrated by the sketch of Fig. 4. Obviously, the total driving force for diffusion across the intermetallic layer ($\Delta\tilde{\mu}_D$) is reduced from its equilibrium value by dissipative loss at the interfaces ($\Delta\tilde{\mu}_l$ and $\Delta\tilde{\mu}_r$):

$$\Delta\tilde{\mu}_D = \Delta\tilde{\mu}_{\mathrm{eq}} - (\Delta\tilde{\mu}_l + \Delta\tilde{\mu}_r). \tag{21}$$

Following Deal and Grove, the compound should have a rather narrow existence range so that the flux within the intermetallic is practically homogeneous ($c_2 \approx c_3 \approx: c_I$). This leads to the exchange fluxes

$$\begin{aligned} \tilde{j}_l &= \rho\sqrt{c_1(1-c_1)c_2(1-c_2)}\cdot\kappa_l\frac{\Delta\tilde{\mu}_l}{\mathrm{k}T} \\ \tilde{j}_D &= \rho c_I(1-c_I)\frac{D}{w}\frac{\Delta\tilde{\mu}_D}{\mathrm{k}T} \\ \tilde{j}_r &= \rho\sqrt{c_3(1-c_3)c_4(1-c_4)}\cdot\kappa_r\frac{\Delta\tilde{\mu}_r}{\mathrm{k}T} \end{aligned} \tag{22}$$

through the left boundary, across the intermetallic phase, and through the right boundary, respectively. κ_l and κ_r are defined here in analogy to the diffusion coefficient. They quantify the exchange flux between A and B atoms but exclude thermodynamic factors except configurational entropy (as D, also κ_l and κ_r may depend on composition). In bulk diffusion, the local compositions before and after a jump remain practically the same, which leads to the concentration prefactor $c(1-c)$, well known in the formulation of

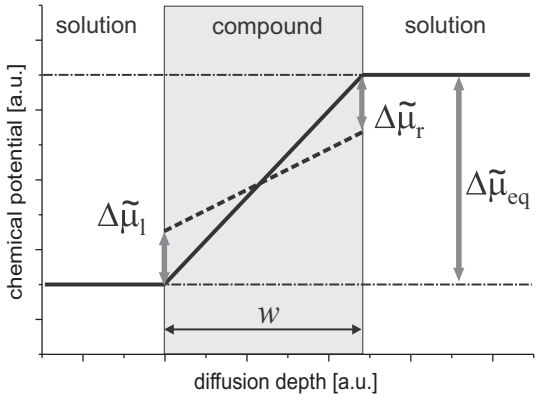

Fig. 4. Schematic interdiffusion potentials across the diffusion zone for the case of unlimited fast interfacial transport (solid line) and the case of interface control (dashed). The compositions of the terminating solutions are assumed to match the respective equilibrium value c_1 and c_4. So deviation from equilibrium appears only inside the compound. Total driving force $\Delta\mu_{\mathrm{eq}}$ and the losses at the interfaces ($\Delta\mu_l$, $\Delta\mu_r$) are also indicated.

interdiffusion flux (e.g. Eq. (8)). At the interfaces however, the concentrations on both sides may differ considerably which raises the question how to average the concentration factors appropriately. The first and the third equation make use of the geometric mean, which is justified in the appendix (Appendix C).

After a sufficient transient period, the three fluxes in Eq. (22) must become identical ($\tilde{j}_l = \tilde{j}_D = \tilde{j}_r = \tilde{j}$). By evaluating Eq. (22), we receive for this steady flux

$$\tilde{j} = \rho c_I(1-c_I)\frac{D}{w + \frac{D}{\kappa_{\mathrm{eff}}}}\frac{\Delta\tilde{\mu}_{\mathrm{eq}}}{\mathrm{k}T}, \tag{23}$$

in which the effective barrier coefficient

$$\frac{1}{\kappa_{\mathrm{eff}}} := \sqrt{\frac{c_I(1-c_I)}{c_1(1-c_1)}}\frac{1}{\kappa_l} + \sqrt{\frac{c_I(1-c_I)}{c_4(1-c_4)}}\frac{1}{\kappa_r} \tag{24}$$

has been defined as a convenient abbreviation. The atomic transport leads to the growth of the intermetallic layer

$$\frac{dw}{dt} = \left(\frac{1}{c_2-c_1} + \frac{1}{c_4-c_3}\right)\frac{\tilde{j}}{\rho} \tag{25}$$

$$= \underbrace{\left[\frac{c_I(1-c_I)}{c_2-c_1} + \frac{c_I(1-c_I)}{c_4-c_3}\right]}_{:=\gamma}\cdot\frac{D}{w+\frac{D}{\kappa_{\mathrm{eff}}}}\cdot\frac{\Delta\tilde{\mu}_{\mathrm{eq}}}{\mathrm{k}T} \tag{26}$$

which is integrated to

$$t = \frac{1}{2\gamma D}\frac{\mathrm{k}T}{\Delta\tilde{\mu}_{\mathrm{eq}}}w^2 + \frac{1}{\gamma\kappa_{\mathrm{eff}}}\frac{\mathrm{k}T}{\Delta\tilde{\mu}_{\mathrm{eq}}}w =: \mathbf{A}\cdot w^2 \quad + \quad \mathbf{B}\cdot w \tag{27}$$

to predict the temporal evolution of the layer thickness. The numerical factor γ is close to one (exactly one for a strict line compound between pure phases). Although not accurate in quantitative prediction, the Deal-Grove model clarifies the essential general features: Interfacial barriers (i) slow down the growth and (ii) they introduce a linear regime in the growth kinetics which dominates the initial stages of reaction.

5.2. Treating interfacial barriers by the kinetic simulation

Due to its transparent concept, the kinetic algorithm outlined in Section 2 can easily be extended to include the effect of extra interfacial barriers. In the simulated composition profiles, the interphase boundaries are usually reflected by a single slab with a concentration inside the 'prohibited' two-phase range (see Fig. 2). So in fact, we just have to reduce diffusion into and out of this slab by a certain factor to slow down the transport through the interface. Accordingly, Eq. (6) is modified to

$$\vec{j}_i = -\rho F\mathscr{D}_i c_i\left(\frac{c_v}{\mathrm{k}T}\nabla'\mu_i - \nabla' c_v\right) \quad \text{for } i = 1,\ldots,n \text{ and } i = v, \tag{28}$$

in which the factor F equals one inside the phases but is considerably less in the 'prohibited' concentration ranges. In the generic case of vacancy equilibrium, the latter simplifies to

$$\vec{j}_i = -\rho F D_i^*\frac{c_i}{\mathrm{k}T}\nabla'\mu_i \quad \text{for } i = 1,\ldots,n. \tag{29}$$

(Since interfacial barriers prevent local equilibrium, we have to make use in this case of the chemical potentials rather than the thermodynamic factor, even for a binary system.)

6. Validation of the approach to linear kinetics

Let us check whether the simulation tool so describes a linear-to-parabolic transition in an appropriate manner. We simulate growth for symmetric phase diagrams as in Fig. 1(a). To simplify the quantitative discussion, we matched the initial compositions

of the reaction couples to the respective equilibrium concentrations of the terminating phases (c_1, c_4). In a first calculation, the interaction parameter was increased to $V = 500$ kT to approximate a real line compound (remaining existence range of 0.44 at.%). Identical partial diffusion coefficients and atomic volumes were chosen for both components so that the calculation made use of Eq. (29).

Fig. 5 presents the calculated layer thickness versus diffusion time for different values of the F parameter as stated in the figure. In this double logarithmic plot, the slope clearly identifies the transition from a linear to the parabolic regime. Furthermore, by decreasing F (from $F = 1$ down to $F = 0.001$), the linear regime extends to later stages and the overall growth rate gets reduced. Obviously, the proposed interfacial deceleration factor provides an efficient control of the growth. To demonstrate its quantitative suitability, we evaluate the evolution of the reaction product in terms of the parabolic and linear contributions in Eq. (27). The respective coefficients A and B are determined in dependence on the parameters F and V by fitting Eq. (27) to the simulated phase width.

Results are shown in Fig. 6(a) and (b), respectively. By variation of the curvature of the Gibbs potential ($V = 10$ kT, 20 kT or 500 kT), the composition range of the intermetallic compound is adjusted ($\Delta c = 25.9$ at.%, 11.8 at.%, or 0.44 at.%, respectively).

The "**A**" parameter characterizes the diffusional growth of the intermetallic product at late stages when growth is controlled by volume transport. So, no surprise that it is not effected by the decelaration factor at the interface. This is fully confirmed by the data presented in Fig. 6 (a). Except those points that could not be reliably determined because of a too short parabolic regime (light grey), the data points fall on plateaus that only depend on the underlying phase diagram but not on the F parameter.

An attempt to understand the plateau levels by the Deal-Grove expression Eq. (27) is enlightening. Only for the line compound ($V = 500$ kT) the agreement is satisfying (see solid lines at left hand side of Fig. 6(a)) while significant discrepancy appears for the smaller V. This discrepancy does not represent a failure of the proposed simulation algorithm. It is due to the fact that the Deal-Grove model neglects the variation of the flux across the intermetallic layer. By contrast, a more accurate calculation of the reaction thickness is achieved via the flux at the Matano plane, as illustrated in Fig. 7. Integration of the Matano flux j_M on time equals the total amount of exchanged atoms (material transported from the dark grey region to the light grey region) and thus defines the thickness of the diffusion zone. In very good approximation on Fig. 2 concentration varies linearly across the intermetallic layer so

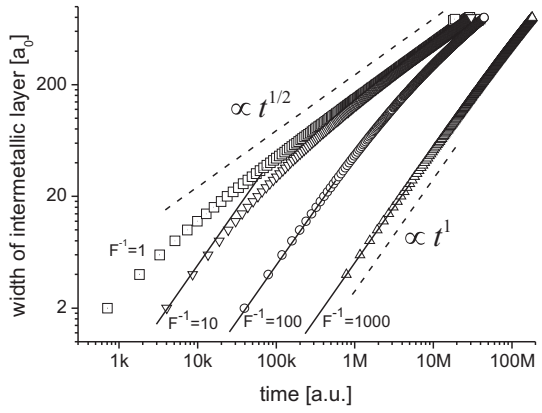

Fig. 5. Kinetic simulation of the growth of an AB compound based on the symmetric phase diagram ($g_0/\mathrm{kT} = 1.2$ and $V/\mathrm{kT} = 500$). By variation of the parameter F (0.001–1), barriers of controlled efficiency are introduced at both interfaces.

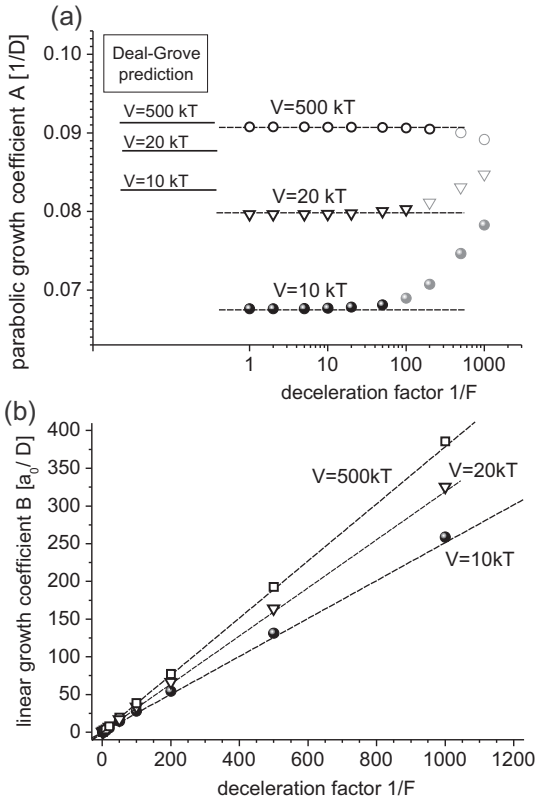

Fig. 6. Evaluation of simulated layer growth on the basis of symmetric phase diagrams with varying stability of the intermetallic. Data points in (a) represent the results for the "**A**" parameter (points in light grey are not reliable due to too small parabolic contribution to the kinetics). For comparison dashed lines represent prediction by Eq. (30). Predictions by the Deal-Grove model (solid lines) are shown on the left. Data points in (b) represent simulation results for the "**B**" parameter. Dashed lines were calculated by Eq. (33).

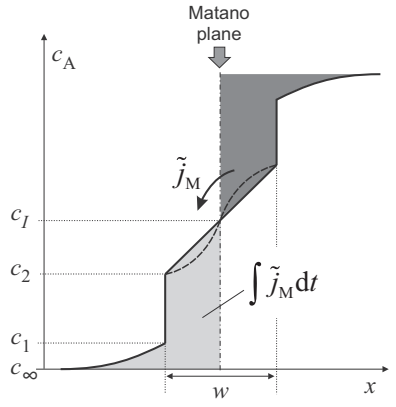

Fig. 7. Principle of growth rate estimation. The integral of the flux across the Matano plane (dashed-pointed) corresponds to the total amount of exchanged atoms (grey). The composition profile across the intermetallic is close to linear but still slightly curved (dashed).

that the light grey area is given by $((c_2 - c_1) + (c_I - c_1))w/4$ (assuming $c_\infty = c_1$). Thus, on the one hand the Matano flux equals

$$\tilde{j}_M(t) = \rho \frac{(c_I - c_1) + (c_2 - c_1)}{4} \cdot \frac{dw}{dt} \tag{30}$$

and on the other, Ficks law requires

$$\tilde{j}_M = \rho c_I (1 - c_I) \frac{D}{w} \frac{\Delta \mu_{eq.}}{kT}. \tag{31}$$

Combining the latter two equations leads to the prediction of "**A**"

$$\mathbf{A} = \frac{1}{2w}\frac{\mathrm{d}t}{\mathrm{d}w} = \frac{c_I + c_2 - 2c_1}{8\,c_I(1-c_I)}\,\frac{1}{D}\,\frac{\mathrm{k}T}{\Delta\mu_{\mathrm{eq.}}}. \tag{32}$$

The latter expression for the parameter "A" is different from that stated in Eq. (27). As expected, both become equal only in the limit $c_2 = c_3 = c_I$. Eq. (32) decribes the plateaus in Fig. 6 already reasonably well. (a careful investigation of the analytical expressions in Section 3 reveals a weak S-shaped curvature of the concentration profiles as illustrated (exaggerated) by the dashed line in Fig. 7. This leads to an increase of j_M of up to 3%. Taking this into account, the values of the parabolic growth parameter "A" derived from the simulation match perfectly the theoretical expectation of Eq. (30), see dashed lines in the figure).

Quantitative results of the "**B**" parameter are presented in Fig. 6 (b). It obviously scales perfectly proportional to $1/F$ for all studied phase diagrams. The variation of the slope $\mathrm{d}B/\mathrm{d}(1/F)$ with the thermodynamic stability of the intermetallic phases (V parameter) is naturally expected, as Eq. (27) suggests

$$\mathbf{B} = \frac{1}{\gamma\kappa_{\mathrm{eff}}}\cdot\frac{\mathrm{k}T}{\Delta\tilde{\mu}_{\mathrm{eq}}} \tag{33}$$

Since $\Delta\tilde{\mu}_{\mathrm{eq}}$ scales inversely with V (5.18 kT,4.72 kT, and 4.39 kT at $V = 10$ kT, 20 kT, and 500 kT, respectively), the observed increase of the slope with V is already understood. Beside the direct dependence on $\Delta\tilde{\mu}_{\mathrm{eq}}$ there is also an implicit dependence of κ_{eff} on the phase boundary concentrations:

$$\kappa_{\mathrm{eff}} = \frac{(2-c_I-c^*)(c_I+c^*)}{8\,c_I(1-c_I)}\,\frac{FD}{a_0}; \quad \text{with} \quad c^* = (c_1+c_2)/2 \tag{34}$$

The "**B**" parameters so predicted by combination of Eqs. (33) and (34) are presented as dashed lines in Fig. 6(b). They are in convincing agreement with the simulated data points. It should be noted that the composition dependence of κ_{eff} stated in Eq. (34) is related to the actual implementation of the simulation algorithm (see Appendix A).

7. An example: Asymmetric arrangement of barriers

Up to now, we considered only situations that could be also understood by phenomenological equations and so to allow the validation of the suggested simulation approach. The kinetic modelling however can handle also complex cases for which the formulation of phenomenological rate equations becomes difficult or even impossible, e.g. situations with many different intermetallic phases, three dimensional geometries, or non-equilibrium vacancies. As a still transparent but already more complex example, we present a set of simulations for the asymmetric phase diagram shown in Fig. 1(b). Since the nature of the interfaces between different phases can be quite different, we may also expect different kinetic barriers. We compare simulations of layer growth, in which either identical barriers at both interfaces, only one barrier at the left or at the right interface, or no barrier at all were present. In all four cases the composition of the reacting materials were fixed to the equilibrium concentrations (c_1, c_4).

Results are shown in Fig. 8. In the latter case (no barriers), exclusive parabolic growth is naturally expected. The other three cases demonstrate a linear regime in the initial stages. The extensions of these linear regimes however are quite different as well as the corresponding growth constants. In particular, the simulation demonstrates that the growth constants depend on whether positioning the single barrier at the left or the right interface, although

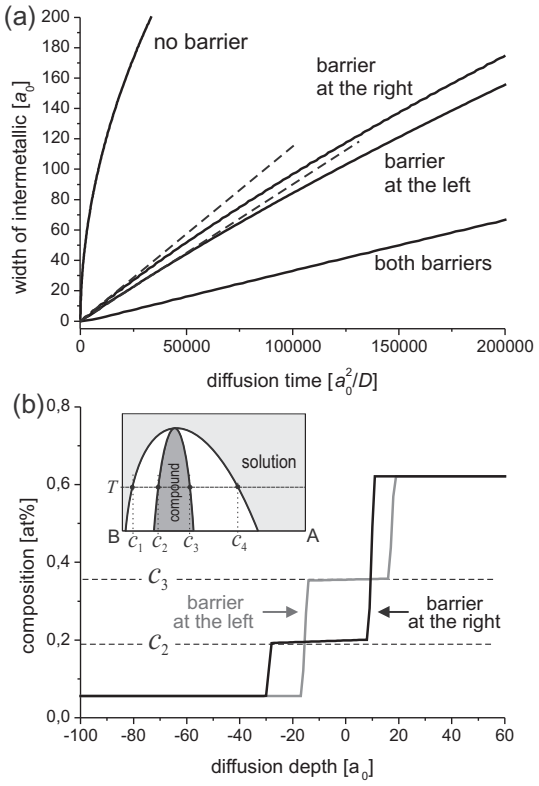

Fig. 8. Simulation of phase growth with asymmetric phase diagram (parameters as in Fig. 1(b)) and arrangement of barriers: (a) Thickness of the formed intermetallic compound versus diffusion time for four different situations: no barrier (pure Fickian diffusion), barriers at both interfaces of the intermetallic, barrier only at the left (low A concentration) or the right side (high A concentration) of the compound. The latter three cases reveal a linear regime in the early stage of growth. The ratio between the corresponding linear growth rates amounts to 1:0.783:0.296 (right: left:both). (b) Simulated composition profiles in the linear regime for the barrier at the left and at the right interface.

the thermodynamic driving force to form the compound is identical.

A quantitative understanding of such phenomena by the Deal-Grove concept is not possible anymore. But qualitative considerations still indicate that the results of the simulation are physically reasonable. Simulated composition profiles of the early linear growth stage demonstrate that for the single barriers (partial Fig. 8(b)), the respective composition of the initial compound is driven fully to the respective opposite boundary, i.e. to high concentration (c_3) when the barrier is positioned at the low concentration interface and vice versa. So in both cases, the full driving force is available for the transport across the interface. Consequently, we can estimate the relative growth rates based on the steady state fluxes. The latter may be derived in analogy to Eq. (A.1) choosing the appropriate $c_I \approx c_2 \approx c_3$. This predicts the ratio between the growth constants to be 0.813 (barrier at the left to barrier at the right case) which has to be compared with the ratio 0.783 found in the simulation (see Fig. 8). A satisfying agreement. (The remaining discrepancy is probably explained by additional curvatures of the composition profiles that are neglected in the estimate but clearly seen in the simulated profiles.).

8. Conclusions

A transparent computational concept of simulating phase formation by reactive diffusion has been presented that does not require pre-defined interfaces to characterize a heterogeneous

microstructure. The equilibrium phases form automatically —via the composition-dependent chemical potentials or appropriate thermodynamic factors. Interfaces are simply marked by a composition inside the thermodynamically 'forbidden' two-phase range. In this work, we validated this concept and extended it so to also describe the effect of interfacial transport barriers.

- To enable a quantitative check, a new analytical transformation of the Fickian equations for interdiffusion couples was derived, that allows treating arbitrary composition-dependent chemical diffusivity as a free input parameter and so can easily be adapted to any binary phase diagram.
- The direct comparison with exact analytical solutions of the reactive diffusion problem in layer geometry confirmed the quantitative correctness of the simulation concept. The predicted absolute thicknesses of the intermediate product layers are in agreement with the analytical description to very high precision.
- By assigning formally a reduced diffusion coefficient to the 'forbidden' two-phase composition ranges of the phase diagram, the kinetic simulation concept fully reproduces the physical features of interfacial transport barriers. The demonstrated inverse proportionality of the reduction factor to the phenomenological barrier coefficient allows a transparent scaling of the barrier effect.
- The quantitative correlation between the reduction factor and the simulated linear growth rate has been established.

Acknowledgments

This work and publication was supported by the OTKA Board of Hungary (NF 101329), by the GINOP-2.3.2-15-2016-00041 project, co-financed by the European Union and the European Regional Development Fund, and the German Science Foundation (DFG, SCHM 1182/9). The work of J.J. Tomán was supported by National Excellence - Campus Hungary program in the framework of TÁMOP 4.2.4.B/2-11/1-2012-0001 project. Furthermore, joint work was made possible by the visiting professor program of University of Muenster in Germany.

Appendix A. Implementation of the simulation algorithm

The model summarized in Section 2 together with the assumptions of equal partial volumes and partial diffusion coefficients of the two species, direct atom exchange, planar geometry, and a constant slab thickness in discretisation lead to the technical procedure used in this work. Local concentrations and chemical potentials are assigned to the slabs, while the diffusion coefficients and currents, as joined properties of two neighboured slabs, are assigned to the interfaces inbetween.

Before starting the simulation, we tabulate the chemical exchange potential on the basis of Section 2.2. The computational cycle of the simulation then: (i) assigns the actual chemical potential according to the composition of the slab by interpolation of the tabulated values; (ii) identifies slabs as interfacial ones by the condition

$$\{c_1 \leqslant c[i] \leqslant c_2 \quad \text{Or} \quad c_3 \leqslant c[i] \leqslant c_4\}$$

At both sides of identified interface slabs, the deceleration factor is set to the desired values i.e. $F[i] = F[i+1] = F$, else it is kept equal to 1; (iii) determines the flux between slabs $[i-1]$ and $[i]$ by

$$c_{av}[i] = \frac{c[i-1] + c[i]}{2}$$

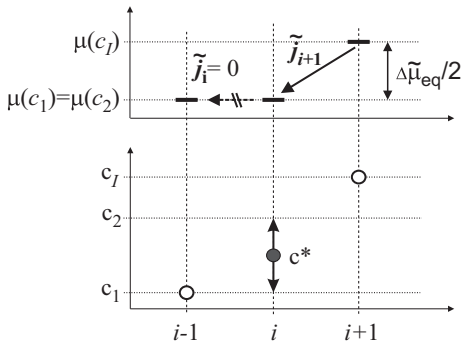

Fig. A.9. Local concentration and flux situation at the grid points close to the interface.

$$\tilde{j}[i] = -\rho F[i] D^* c_{av}[i](1 - c_{av}[i]) \frac{\tilde{\mu}[i] - \tilde{\mu}[i-1]}{a_0},$$

where a_0 is the thickness of one slab; (iv) updates the compositions according to

$$c[i](t + dt) = c[i](t) + \frac{1}{\rho} \frac{\tilde{j}[i] - \tilde{j}[i+1]}{a_0} dt.$$

Composition was kept constant at the outer boundaries of the simulated volume. This boundary condition, however, did not become decisive as the calculated volume was always significantly larger than the extension of the diffusion zone.

With these details of the algorithm, an understanding of the interfacial flux and thus the κ coefficient may be obtained: Compositions, assignment of chemical potentials, and fluxes at the (left) interface are illustrated in Fig. A.9 for the described discretisation scheme. The interface is marked by slab [i] with a concentration within the two phase region. This intermediate composition is fluctuating between c_1 and c_2. On statistical average, we set $c^* = (c_1 + c_2)/2$. The chemical exchange potential is constant for all concentrations in the range c_1 to c_2. So, a driving force only develops by shifting the concentration of slab $[i+1]$ into the phase field of the intermetallic. The maximum possible driving force (in the case of symmetrical phase diagram with symmetrical barriers $\Delta\tilde{\mu}_{eq}/2$) is established in the linear regime if $c[i+1] = c_I$. With this, the flux into the interface slab is found as

$$\tilde{j}_I = \rho \left(\frac{c^* + c_I}{2}\right) \left(1 - \frac{c^* + c_I}{2}\right) \frac{FD}{a_0} \cdot \frac{\Delta\tilde{\mu}_{eq}}{2kT} \tag{A.1}$$

The flux j_i out of the interface slab is blocked, until the concentration inside the interface slab exceeds the boundary composition c_2.

Appendix B. Integration of the analytical equations

The technical procedure of solving the analytical Eqs. (19) and (20) in Section 3 shall be illustrated. Concentration c_M and flux j_M at the Matano plane are first guessed and then iteratively refined to match by integration of Eqs. (19) and (20) the correct terminating concentrations of the diffusion couple far from the Matano plane ("shooting" method to solve a boundary value problem). The detailed steps: The composition-dependent chemical diffusion coefficient has been tabulated. Beginning at the Matano plane, positive and negative halves of the composition profile are calculated separately. The Matano plane be positioned at $x = u = 0$. Composition c_M and composition gradient c'_M at the Matano plane are intuitively guessed and a convenient composition increment Δc is selected. We initialize the integration of the positive half with $x_0 = 0,\ u_0 = 0,\ c_0 = c_M,\ c'_0 = c'_M,\ \tilde{j}_0 = \tilde{D}(c_0)c'_0$. Since Eq. (19) is

undetermined at $u = 0$, the first integration step is different from the following ones. Here the first step is:

$$\begin{aligned} c_1 &= c_0 + \Delta c \\ x_1 &= \Delta c / c_0' \\ u_1 = \Delta c/(c_0' \widetilde{D}^{1/2}(c_0)) \quad &\text{(compare Eq. (16))} \\ \tilde{j}_1 &= \tilde{j}_0 \cdot \exp(-u_1^2/4t) \\ c_1' &= j_1/\widetilde{D}(c_1) \end{aligned}$$

and all subsequent integration steps are:

$$\begin{aligned} c_{i+1} &= c_i + \Delta c \\ x_{i+1} &= x_i + \Delta c/c_1' \\ u_{i+1} &= u_i + (x_i/u_i)(\Delta c/j_1) \\ j_{i+1} &= j_0 \exp(-u_{i+1}^2/4t) \\ c_{i+1}' &= j_{i+1}/\widetilde{D}(c_i) \end{aligned}$$

which are performed until the right boundary of the diffusion couple has been reached. The treatment of the negative half of the profile follows by analogy. Then, the limit compositions far from the Matano plane are compared with the desired boundary values. Composition c_M and composition gradient c_M' at the Matano plane are accordingly adjusted in further integration trials, until the boundary conditions are matched at both sides of the diffusion couple.

Appendix C. Justification of geometric average of composition factors

The statistical concentration factors in the expressions of the interface fluxes in Eq. (22) can be justified in the following way: The Deal-Grove concept only considers exchange flux (vanishing drift terms). The probability of an A-B exchange across the interface must be proportional to the concentrations of the respective species on both sides. Thus, assuming thermally activated jumps over a barrier, we expect for the exchange flux of an A atom to the right and a B atom to the left:

$$\begin{aligned} j_{A,B} &\propto c_1 \cdot \exp\left(\frac{E_1^A - E_2^A}{2kT}\right) \cdot (1-c_2) \cdot \exp\left(\frac{E_2^B - E_1^B}{2kT}\right) \\ &= \sqrt{c_1 \cdot c_2} \cdot \exp\left(\frac{E_1^A + kT\ln c_1 - E_2^A - kT \ln c_2}{2kT}\right) \times \\ &\sqrt{(1-c_1)(1-c_2)} \cdot \exp\left(\frac{E_2^B + kT\ln(1-c_2) - E_1^B - kT\ln(1-c_1)}{2kT}\right) \\ &= \sqrt{c_1(1-c_1)\cdot c_2(1-c_2)} \cdot \exp\left(\frac{\mu_1^A - \mu_2^A + \mu_2^B - \mu_1^B}{2kT}\right). \end{aligned} \tag{C.1}$$

Vice versa for the exchange of B to the right and A to the left:

$$\begin{aligned} j_{B,A} &\propto (1-c_1) \cdot \exp\left(\frac{E_1^B - E_2^B}{2k_BT}\right) \cdot c_2 \cdot \exp\left(\frac{E_2^A - E_2^A}{2kT}\right) \\ &= \sqrt{c_1(1-c_1)c_2(1-c_2)} \cdot \exp\left(\frac{\mu_1^B - \mu_2^B + \mu_2^A - \mu_1^A}{2kT}\right). \end{aligned} \tag{C.2}$$

In these equations, the indexes $i = 1, 2$ stand for the right and left side of the interface, respectively, while E_i^A or E_i^B denotes the respective site energy of species A or B. The saddle point energy is assumed as $E_s = \Delta E + (E_1 + E_2)/2$ with a kinetic constant ΔE. The balance of these partial fluxes yields the total exchange flux, which reads

$$\begin{aligned} \tilde{j} &= j_{A,B} - j_{B,A} \\ &\propto \sqrt{c_1(1-c_1)c_2(1-c_2)} \\ &\quad \cdot \left[\exp\left(\frac{\tilde{\mu}_1 - \tilde{\mu}_2}{2kT}\right) - \exp\left(-\frac{\tilde{\mu}_1 - \tilde{\mu}_2}{2kT}\right)\right] \\ &\approx \sqrt{c_1(1-c_1)c_2(1-c_2)} \cdot \frac{\tilde{\mu}_1 - \tilde{\mu}_2}{kT} \\ &= -\sqrt{c_1(1-c_1)c_2(1-c_2)} \cdot \frac{\Delta\tilde{\mu}}{kT}. \end{aligned} \tag{C.3}$$

The last expression is the direct analog to the interface fluxes in Eq. (22).

References

[1] A. Borgenstam, A. Engstrom, L. Hoglund, J. Agren, Dictra, a tool for simulation of diffusional transformations in alloys, J. Phase Equilib. 21 (2000) 269–280.
[2] J. Svoboda, E. Gamsjäger, F.D. Fischer, P. Fratzl, Application of the thermodynamic extremal principle to the diffusional phase transformations, Acta Mater. 52 (2004) 959–967.
[3] Z. Erdélyi, G. Schmitz, Reactive diffusion and stresses in spherical geometry, Acta Mater. 60 (4) (2012) 1807–1817.
[4] H. Larsson, H. Strandlund, M. Hillert, Unified treatment of kirkendall shift and migration of phase interfaces, Acta Mater. 54 (2006) 945–951.
[5] J. Philibert, Atom Movements, Diffusion and Mass Transport in Solids, Les Edition des Physiques, 1991.
[6] Z. Balogh, G. Schmitz, Diffusion in solids, in: D.E. Laughlin, K. Hono (Eds.), Physical Metallurgy, Elsevier, 2014.
[7] B.E. Deal, A.S. Grove, General relationship for the thermal oxidation of silicon, J. Appl. Phys. 36 (12) (1965) 3770–3778.
[8] U. Gösele, K.N. Tu, Growth kinetics of planar binary diffusion couples: thin film case versus bulk cases, J. Appl. Phys. 53 (4) (1982) 3252–3260.
[9] W.C. Johnson, Effect of interfacial kinetic barriers on interface motion in binary diffusion couples, Metall. Mater. Trans. A 29A (1998) 2021–2032.
[10] B.P. M. Millares, E. Lelievre, Multiphase reaction-diffusion in the au-in system, Scripta Met. Mater 27 (1992) 1777–1782.
[11] J.Y. Cheng, L.J. Chen, Growth kinetics of amorphous interlayers by solid-state diffusion in ultrahigh vacuum deposited polycrystalline nb and ta thin films on (111)si, J. Appl. Phys. 69 (1991) 2161–2168.
[12] F. Nemouchi, D. Mangelinck, C. Bergman, P. Gas, U. Smith, Differential scanning calorimetry analysis of the linear parabolic growth of nanometric ni silicide thin films on a si substrate, Appl. Phys. Lett. 86 (2005) 041903.
[13] C. Cserhati, Z. Balogh, A. Csik, G.A. Langer, Z. Erdélyi, G. Glodán, et al., Linear growth kinetics of nanometric silicides in co/amorphous-si and co/cosi/amorphous-si thin films, J. Appl. Phys. 104 (2008) 024311.
[14] B. Parditka, M. Verezhak, Z. Balogh, A. Csik, G.A. Langer, D.L. Beke, et al., Phase growth in an amorphous sicu system, as shown by a combination of snms, xps, xrd and apt techniques, Acta Mater. 61 (2013) 7173–7179.
[15] A. Gusak, T. Zaporozhets, Y. Lyashenko, S. Kornienko, O. Pasichnyy, A. Shirinyan, Diffusion-Controlled Solid State Reactions: in Alloys, Thin-Films, and Nanosystems, John Wiley & Sons, 2010, ISBN 978-3527408849.
[16] Y.H. Yung-Chen Lin Yu Chen, The growth and applications of silicides for nanoscale devices, Nanoscale 4 (2012) 1412–1421.
[17] J. Tomán, C. Cserháti, Y. Iguchi, Z. Jánosfalvi, Z. Erdélyi, Investigation of the role of vacancy sources and sinks on the Kirkendall-effect on the nanoscale, Thin Solid Films 591 (Part B) (2015) 363–367.
[18] J. Svoboda, F. Fischer, Modelling of the influence of the vacancy source and sink activity and the stress state on diffusion in crystalline solids, Acta Mater. 59 (3) (2011) 1212–1219.
[19] Y. Mishin, J.A. Warren, R.F. Sekerka, W.J. Boettinger, Irreversible thermodynamics of creep in crystalline solids, Phys. Rev. B 88 (2013) 184303.
[20] G.B. Stephenson, Deformation during interdiffusion, Acta Metall. 36 (10) (1988) 2663–2683.
[21] H. Mehrer, Diffusion in Solids, Springer-Verlag, Berlin Heidelberg, 2007.
[22] J. Svoboda, F. Fischer, A new computational treatment of reactive diffusion in binary systems, Comput. Mater. Sci. 78 (2013) 39–46.
[23] F. Fischer, J. Svoboda, Diffusion of elements and vacancies in multi-component systems, Prog. Mater. Sci. 60 (0) (2014) 338–367.
[24] G.V. Kidson, Some aspects of the growth of diffusion layers in binary systems, J. Nucl. Mater. 3 (1961) 21–29.
[25] B. Parditka, J. Tomán, C. Cserháti, Z. Jánosfalvi, A. Csik, I. Zizak, et al., The earliest stage of phase growth in sharp concentration gradients, Acta Mater. 87 (2015) 111–120.